International Journal of Fatigue 172 (2023) 107645

Contents lists available at ScienceDirect

International Journal of Fatigue

journal homepage: www.elsevier.com/locate/ijfatigue

Fatigue life prediction based on a deep learning method for Ti-6Al-4V fabricated by laser powder bed fusion up to very-high-cycle fatigue regime

Yinfeng Jia [a,1], Rui Fu [a,1], Chao Ling [a], Zheng Shen [b], Liang Zheng [a,*], Zheng Zhong [a,*], Youshi Hong [c]

[a] School of Science, Harbin Institute of Technology (Shenzhen), Shenzhen, China
[b] R & D Center, CRRC Zhuzhou Electric Co., Ltd, Zhuzhou, Hunan, China
[c] LNM, Institute of Mechanics, Chinese Academy of Sciences, Beijing, China

ARTICLE INFO

Keywords:
Fatigue life prediction
Deep learning method
Laser powder bed fusion
Ti-6Al-4V
Very-high-cycle fatigue

ABSTRACT

Microstructural defects and inhomogeneity of titanium alloys fabricated by laser powder bed fusion (LPBF) make their fatigue behaviors much more complicated than the conventionally made ones, especially in very-high-cycle fatigue (VHCF) regime. Most of traditional models/formulae and currently-used machine learning algorithms mainly concern fatigue behavior of LPBF-fabricated titanium alloys in high-cycle fatigue (HCF) regime, but rarely in VHCF regime. In this paper, a deep belief neural network-back propagation (DBN-BP) model was proposed to predict the fatigue life of LPBF-fabricated Ti-6Al-4V up to VHCF regime. Results obtained in this study indicate that the DBN-BP model exhibits high precision and strong stability in predicting the fatigue life of LPBF-fabricated Ti-6Al-4V in both HCF and VHCF regimes. The primary hyperparameters of the DBN-BP model were optimized to further improve the prediction precision of this innovative model. Finally, the optimal DBN-BP model was applied to predict the relation between mean stress and stress amplitude, and the effect of energy density on the fatigue behavior of LPBF-fabricated Ti-6Al-4V up to VHCF regime.

1. Introduction

Fatigue life prediction is a crucial issue in the fatigue research of metallic materials. In the past decades, researchers have developed various methods to predict the fatigue lives of metallic materials, e.g., the empirical formula based on fracture mechanics [1-3], the fatigue damage evolution models based on continuous damage mechanics [4-6], and the probabilistic models combining the statistical theory and the stress/strain-life curve [7-9]. These models/formulae are either based on the analysis of the experimental results or based on theoretical models with each of them mainly considering some factors. The machine learning (ML) approach is an innovative technique emerging in recent years, which is capable of identifying the influence of different factors on fatigue properties of metallic materials effectively and efficiently, and thus it has been widely applied to fatigue life prediction of various metallic materials [10-12]. The most commonly used ML models include artificial neural network (ANN), support vector regression (SVR) and random forest (RF) [13-16], with each of them having its own strengths and weaknesses. ANN has the advantages of excellent nonlinear fitting ability, simple model and short time consumption [17], but the random generation of the weight and threshold of each layer makes ANN easy to fall into local minimum, causing unstable prediction results [18]. In addition, the network structure parameters of ANN are mainly determined based on the priori knowledge, which makes the predicted results easy to fall into overfitting or failure to converge [19]. SVR with different kernel functions is widely utilized in regression estimation and reliable prediction results can be obtained even with a small amount of data [20,21]. However, SVR is prone to cause overfitting and slow training speed when facing problems with big data or numerous factors [22,23]. Besides, the prediction precision of SVR will be very low when there are some values missing in the fatigue data [24]. RF has strong ability of generalization to unfamiliar data and is not easily affected by missing data [25,26], but it is usually time-consuming due to its complex algorithm and it is prone to cause overfitting when big noise exists in the data [27].

Laser powder bed fusion (LPBF) is one of the most widely used

* Corresponding authors.
E-mail addresses: icon_lzheng@hit.edu.cn (L. Zheng), zhongzheng@hit.edu.cn (Z. Zhong).
[1] These authors contributed equally to this work and should be considered co-first authors.

https://doi.org/10.1016/j.ijfatigue.2023.107645
Received 8 December 2022; Received in revised form 2 March 2023; Accepted 15 March 2023
Available online 20 March 2023

additive manufacturing techniques for metallic materials having the excellent capability of fabricating complex and sophisticated metal components with great efficiency and immense flexibility [28-30]. Titanium alloys fabricated by LPBF process have been broadly utilized in various fields such as aerospace, energy and biomedicine due to their superior strength and excellent corrosion resistance [31,32]. Nevertheless, a certain number of microstructural defects (e.g., pores, lack-of-fusion defects and surface defects) and inhomogeneous microstructures of LPBF-fabricated titanium alloys are generated during the LPBF process, which makes their fatigue behaviors and properties much more complicated to investigate than conventionally manufactured titanium alloys [33-36]. These microstructural defects may be partially eliminated by heat treatment or hot isostatic pressing (HIP), but some of them will be still remained in the materials [37-39]. Several ML models including ANN, SVR and RF have been employed to predict the fatigue lives of LPBF-fabricated titanium alloys (e.g., Ti-6Al-4V) [1,40,41]. However, most of current investigations mainly concern the fatigue lives of these LPBF-fabricated titanium alloys in HCF regime, but rarely in VHCF regime. In fact, the behaviors and mechanisms of crack initiation in VHCF regime, such as the formation of rough area and fish eye, are quite different from those in HCF regime [42-44], which requires to propose an innovative model to address this emerging challenge.

A deep learning model is essentially an improvement of ANN with two or more hidden layers, which has a superior ability to analyze original input data with multiple levels of feature extraction. For LPBF-fabricated titanium alloys in VHCF regime, fatigue life prediction results would be more precise if more fatigue-relevant features can be extracted from the raw data of fatigue testing. In the abovementioned machine learning models, the input features are only randomly sampled by RF [45], simply kernel transformed by SVR [46], neither processed nor transformed by ANN. None of these models are able to conduct deep extraction of the raw fatigue data. Nevertheless, the deep learning model is capable of both extracting and transforming the input features in VHCF regime such that more fatigue-relevant features can be obtained and consequently the prediction results of the fatigue life will be much more precise. As a newly emerged technique, deep learning has been mainly applied to the areas of artificial intelligence and big data mining, but only very few studies concerning fatigue life prediction of metallic materials were reported [47,48], involving neither LPBF-fabricated titanium alloys nor VHCF issues.

In this paper, a deep learning model was employed to predict the fatigue life of LPBF-fabricated Ti-6Al-4V up to VHCF regime. The fatigue data were acquired via a series of fatigue tests considering the effects of various factors, e.g., printing parameters, tensile strength, and fatigue load on the fatigue life of LPBF-fabricated Ti-6Al-4V. Since the fatigue dataset is relatively small and the number of influencing factors is relatively large, a deep learning model, named the deep belief neural network-back propagation (DBN-BP) model proposed by Hinton [49,50], was employed to predict the fatigue life of LPBF-fabricated Ti-6Al-4V up to VHCF regime. The prediction results were then compared with the experimental results to validate this innovative deep learning model. The framework of this paper is as follows. Section 2 introduces the experimental work including the preparation of experimental materials and fatigue tests. Section 3 describes the preprocessing of fatigue data, the establishing and the evaluation of the DBN-BP model. Results and discussion are given in Section 4, and conclusions gained in this study are summarized in Section 5.

2. Construction of raw dataset

2.1. Tensile and fatigue tests

The material investigated in this research was LPBF-fabricated Ti-6Al-4V, a typical additively manufactured titanium alloy with high strength and fracture toughness, low density, and good biocompatibility [31,32,51]. All specimens were fabricated by a LPBF machine (SLM125). The pre-alloyed Ti-6Al-4V powder produced by gas atomization in argon atmosphere and the chemical composition (wt.%) is 5.93Al, 4.01 V, 0.09O, 0.01 N, 0.01C and balance Ti. Most of Ti-6Al-4V powder particles are spherical and the mean diameters of the particles is 45 μm (d50). During the LPBF process, the laser beam was employed to quickly melt the Ti-6Al-4V powder particles layer by layer in an argon-filled chamber and the main processing parameters are laser power 325 W, scan speed 1300 mm/s, layer thickness 0.03 mm and hatch spacing 0.12 mm. Fig. 1a shows that all specimens were produced in the vertical orientation and the laser travelling direction was rotated by 30° for the subsequent layer to minimize the anisotropy of LPBF Ti-6Al-4V specimens. Two kinds of LPBF Ti-6Al-4V specimens were considered for the fatigue testing. One is the as-built specimen that was directly printed according to the shape and dimensions illustrated in Fig. 1b. The other is the surface-polished specimen that was initially printed as a cylindrical bar and then machined and polished, with the shape and dimensions shown in Fig. 1c. Note that the design of ultrasonic fatigue specimens satisfies the resonant condition for 20 kHz testing frequency. In order to reduce the residual stresses induced during LPBF process, a post-LPBF heat treatment was performed by heating at 600 ℃ for 2 h and then air-cooled to room temperature. The chemical composition (wt.%) of the L-PBF Ti-6Al-4V specimens was analyzed by X-ray photoelectron spectroscopy (XPS, ESCALAB 250Xi, Thermo Fisher, UK) and the results were 6.02Al, 3.97 V, 0.10O, 0.01 N, 0.01C and balance Ti. The densities of the LPBF Ti-6Al-4V samples were measured by using Archimedes method [52] to give 4.374 g/cm^3 for as-built samples and 4.382 g/cm^3 for surface-polished samples.

Tensile tests were performed to obtain ultimate tensile strength and yield strength (at 0.2% offset) of LPBF-fabricated Ti-6Al-4V in which gage length and diameter of the tensile test specimen are 20 mm and 5 mm, respectively. During the test, an extensometer was first assembled at both ends of the gage section, and then the testing machine uniformly stretched the specimen at room temperature with a strain rate of 10^{-4} s^{-1} until failed. The stress–strain curve was automatically obtained through the testing machine. Fatigue tests were performed on an ultrasonic axial vibration machine (Lasur GF20-TC) at the frequency of 20 $\pm$ 0.5 kHz, which was installed in a tensile machine (capacity 20 kN) to let the ultrasonic cycling under a given mean stress thus to provide required stress ratio. A compressed gas device was used to cool the fatigue testing specimen to substantially reduce the temperature rise of the specimen. A set of fatigue tests with five stress ratios ($R = -1$, -0.5, 0.1, 0.5 and 0.7) were designated to investigate the effect of stress ratio on the fatigue behavior of the LPBF-fabricated Ti-6Al-4V. The applied stress amplitude of the test specimens is in the range of 50 to 350 MPa. The numbers of the test specimens are 180, 12, 10, 31 and 17 at $R = -1$, -0.5, 0.1, 0.5 and 0.7, respectively. The fractographic morphologies of failed specimens were examined by scanning electron microscopy (SEM, FEI Apreo S, US). The equivalent sizes and shapes of crack initiation region and defects on the observed fracture surfaces were measured by using Image-Pro Plus 6.0 software. More details about material preparation and fatigue testing can be found in Ref [53,54].

2.2. Selection of input and output features

The predicted fatigue life, defined as the number of cycles to fatigue failure, of LPBF-fabricated Ti-6Al-4V is the sole output feature in this deep learning model. The selection of input features is crucial since it directly determines the precision and efficiency of the deep learning model. Fatigue behavior has been intensively investigated in recent years and numerous studies indicated that the fatigue life of LPBF-fabricated Ti-6Al-4V is primarily affected by printing parameters, minimum diameter of specimen, powder size, post-treatment process and loading modes [55-57]. With a combined consideration of the literature review and the authors' prior experimental results [53,54,58,59], the following input features were considered in this deep learning model: stress amplitude σ_a defined as the half of the difference between the

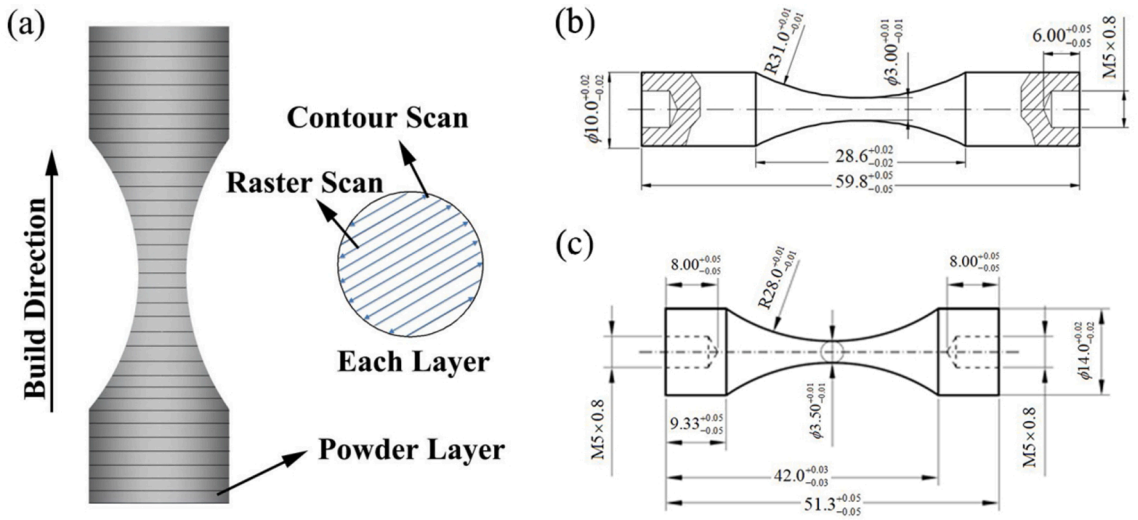

Fig. 1. (a) Build direction and printing strategy of the LPBF process, shape and dimensions (mm) of (b) as-built and (c) surface-polished fatigue test specimens.

maximum and minimum stresses, yield strength σ_y defined as the amount of stress that results in a plastic strain of 0.2%, stress ratio R defined as the quotient of the minimum stress over the maximum stress, diameter D defined as the minimum diameter of the fatigue specimen, powder size L defined as the mean diameter of Ti-6Al-4V powder particles, laser power P defined as the power of the laser beam applied in the LPBF process, scan speed V defined as the travelling speed of the laser beam applied in the LPBF process, layer thickness d defined as the layer height of each successive addition of used Ti-6Al-4V powder particles in the LPBF process, and hatch spacing h defined as the distance between two consecutive laser beams. As stated in Ref.[53], the input energy density E can be utilized to describe the effects of the printing parameters (P, V, d and h) on the fatigue life of LPBF-fabricated Ti-6Al-4V, which is written as [60]:

$$E = \frac{P}{V \times d \times h} \tag{1}$$

Hence, the input features in the deep learning model are composed of stress amplitude σ_a, yield strength σ_y, stress ratio R, minimum diameter of specimen D, powder size L, and input energy density E.

2.3. Raw data collection

The raw data consists of a total number of 250 *S-N* data points collected from the authors' published papers [53,54,58,59]. The values of the selected six input features are listed in Table 1.

3. Fatigue life prediction model

In this study, a deep learning model, named the DBN-BP model, was adopted to predict the fatigue life of LPBF-fabricated Ti-6Al-4V up to VHCF regime. The schematic of the fatigue life prediction, as shown in Fig. 2, is comprised by three steps: data pre-processing, establishing of the DBN-BP model, and model evaluation. It is worth noting that the DBN-BP model consists of two parts, i.e., the Restricted Boltzmann Machines (RBMs) structure for the pre-training process and the BP neural network (BPNN) for the fine-tuning process (Detailed definitions and network structures implemented in the pytorch package are shown in Section 3.2.2, where the codes for DBN and RBM are derived from Ref. [61]). During the pre-training process, the network parameters of each layer in the DBN-BP model were obtained via the use of RBMs to ensure that the mapping relationship of each individual layer reaches the local optimum. Then in the subsequent fine-tuning process, the obtained network parameters were tuned by using BPNN, such that the mapping relationship of the entire network, from the input layer to the output layer, reaches the global optimum.

Table 1
Values of input features, collected from Refs. [53,54,58,59].

No.	D (mm)	L (μm)	E (J/mm^3)	σ_y (MPa)	σ_a (MPa)	R	Refs.
1	3.5	34	47.6	1176 ± 73	145 to 290	−1	[58]
2	3.5	34	26.7	1117 ± 31	100 to 205	−1	[58]
3	3.5	34	19.2	514 ± 30	85 to 175	−1	[58]
4	3.5	34	41.0	1135 ± 25	145 to 290	−1	[58]
5	3.5	34	63.5	1189 ± 43	160 to 290	−1	[58]
6	3.5	34	22.2	1071 ± 58	115 to 290	−1	[58]
7	3.5	34	83.3	1018 ± 20	200 to 350	−1	[58]
8	3.5	34	28.5	960 ± 9	130 to 190	−1	[58]
9	3.5	34	47.6	1089 ± 15	130 to 205	−1	[58]
10	3.5	34	76.0	1045 ± 5	230 to 350	−1	[59]
11	3.5	34	76.0	1045 ± 5	88 to 199	0.5	[59]
12	3.5	45	69.0	1191 ± 20	160 to 306	−1	[53]
13	3.5	45	69.0	1191 ± 20	80 to 180	−0.5	[53]
14	3.5	45	69.0	1191 ± 20	70 to 150	0.1	[53]
15	3.5	45	69.0	1191 ± 20	70 to 105	0.5	[53]
16	3.0	45	69.0	1068 ± 15	50 to 167	−1	[54]
17	3.0	45	69.0	1068 ± 15	100 to 160	0.7	[54]

3.1. Data pre-processing

3.1.1. Normalization and correlation analysis of input features

As listed in Table 1, the input features have different units and magnitudes. Direct training of the DBN-BP model using these original fatigue data could significantly increase the training time and the difficulty to converge. In order to avoid this outcome, the fatigue data need to be normalized into a range [0, 1] by using of Eq. (2).

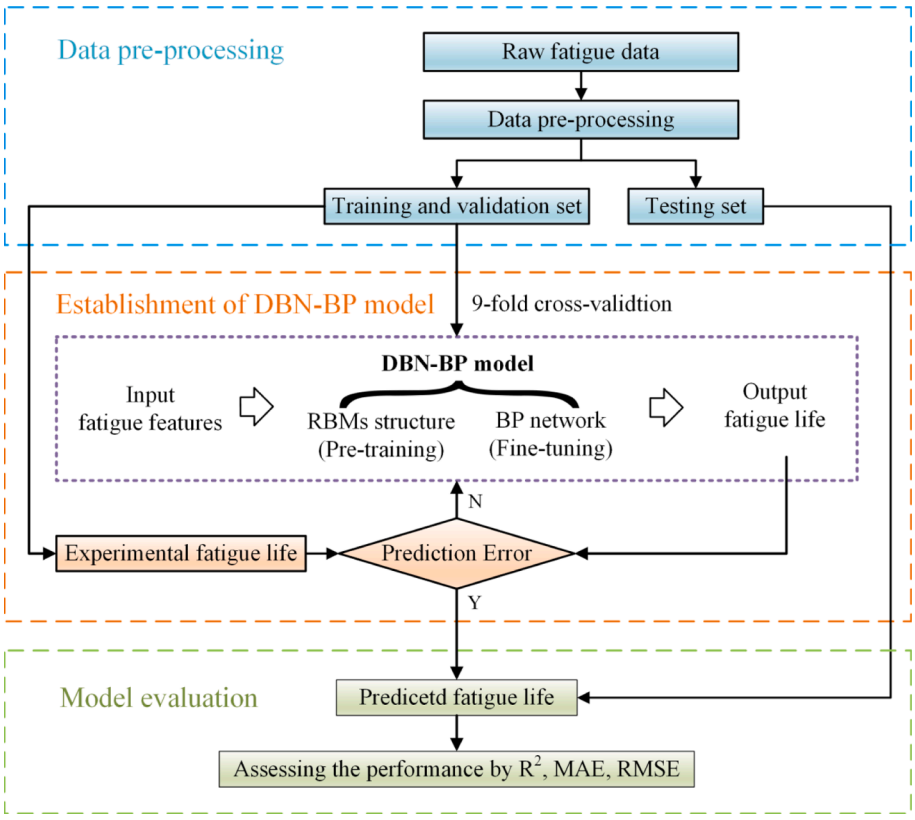

Fig. 2. The schematic of the fatigue life prediction.

$$X^* = \frac{X - X_{\min}}{X_{\max} - X_{\min}} \tag{2}$$

where X is the original value, X^* is the normalized value, $X_{\min}$ and $X_{\max}$ are the minimum and maximum values, respectively.

After normalization, the Pearson correlation analysis was conducted to determine the correlation between the input features, by using the formula of:

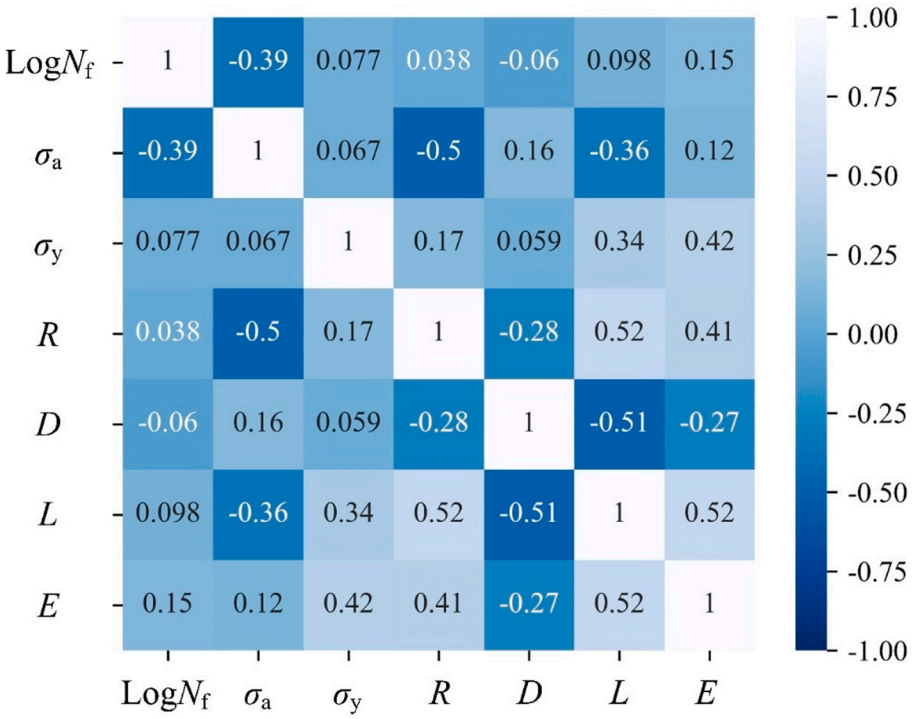

Fig. 3. Pearson correlation heatmap between the six input features.

$$\eta = \frac{\mathrm{cov}(X_1, X_2)}{\sqrt{\mathrm{var}(X_1)\cdot\mathrm{var}(X_2)}} \tag{3}$$

where X_1 and X_2 represent any two of these six input features, cov(·) is the covariance function, var(·) is the variance function.

Pearson correlation heatmap of the six input features is illustrated in Fig. 3 in which none of the values in the correlation coefficient matrix is greater than 0.6, indicating that none of these six input features are strongly correlated. Therefore, these input features could be used as independent variables in the DBN-BP model.

3.1.2. Partition of fatigue dataset

In order to ensure the reliability and generalization ability of the DBN-BP model, the fatigue dataset was randomly divided into training set, validation set and testing set in the ratio of 8:1:1. First, the fatigue life prediction model was obtained through repeated training via the use of the data in the training set; Second, the hyperparameters of the model were optimized by using the data in the validation set; Last, the prediction performance of the model was assessed by comparing with the "unseen/blinded" experimental data in the testing set. If the predicted results agree well with the "unseen/blinded" experimental data, then the prediction performance is considered to be good and thus this model can be used as a predictive model.

Since the randomness of the dataset partition often affects the prediction results of the model, the *k*-fold cross-validation was needed. Because the fatigue data in the training and validation sets were divided into nine equal pieces, so *k* was set to 9 to acquire a reliable validation. To conduct the 9-fold cross-validation, the fatigue data in the training and validation sets were partitioned for 9 times. At each time, the fatigue data in the training and validation sets were randomly divided into 9 equal folds, with eight folds used as the training set and the remaining fold used as the validation set. Then, the prediction results were obtained by taking the average value of the 9 predictions. Hence, the effect of the randomness of the dataset partition on the prediction performance can be diminished via the use of *k*-fold cross validation.

3.2. Establishment of DBN-BP model

As a deep learning model, the DBN-BP model is a modification and improvement of the BPNN model in which a pre-training process is added before the training process. It can be shown later that it is able to well predict the fatigue life of LPBF-fabricated Ti-6Al-4V in both HCF and VHCF regimes. More details about BPNN and DBN-BP models are presented as follows.

3.2.1. BPNN model

As a typical neural network, the BPNN model has been widely used in fatigue life prediction of metallic materials due to its simple structure and high efficiency [41,62]. A typical BPNN model is composed of three parts: an input layer, one or several hidden layers, and an output layer. Fig. 4 illustrates the structure of a generic BPNN model with a single hidden layer. The hyperparameters in the BPNN model, including number of hidden layers, number of nodes in hidden layer, batchsize, learning rate and epoch, are to be initialized and optimized in Section 3.2.3.

As described in Section 3.1, the input features are σ_a, σ_y, R, D, L and E, and the output is the predicted fatigue life of LPBF-fabricated Ti-6Al-4 V, N_{pre}. The input value y and output value o of the hidden layer are presented in Eqs. (4) and (5), and the output value N_{pre} of the output layer is presented in Eq. (6), respectively, in which [x] denotes the input features, $[w]^{(1)}$ represents the weight between the input and hidden layers, $[w]^{(2)}$ represents the weight between the hidden and output layers, $[b]^{(1)}$ and $[b]^{(2)}$ denote the biases of the input and hidden layers, respectively. An activation function $f(\cdot)$ was needed to conduct the nonlinear transformation for the neuron (i.e., the hidden layer) from the input value y to the output value o. The ReLU function is one of the most widely used

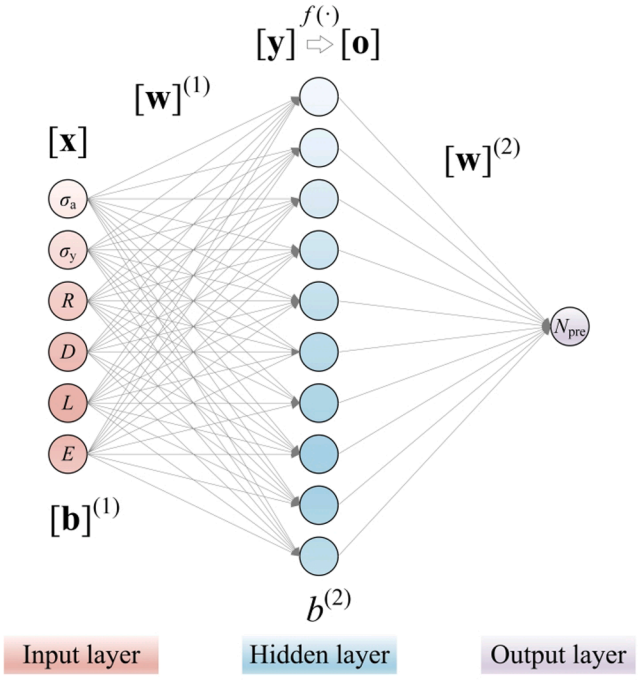

Fig. 4. The structure of a BPNN model with a single hidden layer.

activation functions, which has the advantages of avoiding gradient vanishing [63,64]. Therefore, the ReLU function was applied in this BPNN model, as shown in Eq. (7).

$$[\mathbf{y}] = [\mathbf{w}]^{(1)}[\mathbf{x}] + [\mathbf{b}]^{(1)} \tag{4}$$

$$[\mathbf{o}] = f([\mathbf{w}]^{(1)}[\mathbf{x}] + [\mathbf{b}]^{(1)}) \tag{5}$$

$$N_{pre} = [\mathbf{w}]^{(2)}[\mathbf{o}] + [b]^{(2)} \tag{6}$$

$$f(x) = \begin{cases} 0 & \text{for} \quad x < 0 \\ x & \text{for} \quad x \geq 0 \end{cases} \tag{7}$$

3.2.2. DBN-BP model

The DBN-BP model is the modification and improvement of the BPNN model by integrating the DBN algorithm [49,50]. Composed of stacked layers of Restricted Boltzmann Machines (RBMs), DBN is served as an unsupervised pre-training process whose results are utilized to conduct the subsequent supervised fine-tuning process via the use of BPNN. Fig. 5 illustrates the structure of a generic DBN-BP model in which each RBM consists of a visible layer and a hidden layer that the hidden layer of current (*i*th) RBM is the visible layer of the next ($(i+1)$ th) RBM. The hyperparameters in the DBN-BP model, consisting of number of hidden layers, number of nodes in hidden layer, batchsize, learning rate of pre-training, learning rate of fine-tuning, epoch of pre-training and epoch of fine-tuning, are to be initialized and optimized in Section 3.2.3.

As shown in Fig. 6, a restricted Boltzmann machine (RBM) has a two-layer network structure that consists of a visible layer, which is often called the input layer, and a hidden layer, which is the feature extraction layer. The visible layer and the neurons of the hidden layer are fully connected and bidirectional. The weight w between any two neurons denotes the connection strength, a represents the visible layer bias coefficient, b denotes the hidden layer bias coefficient, $v = (v_1, v_2, \ldots, v_{nv})$ and $h = (h_1, h_2, h_3, \ldots, h_{nh})$ represent the input vector and the output vector, respectively.

RBM is essentially a probabilistic model based on a scalar energy which is defined to quantify the state of the network. When the energy is

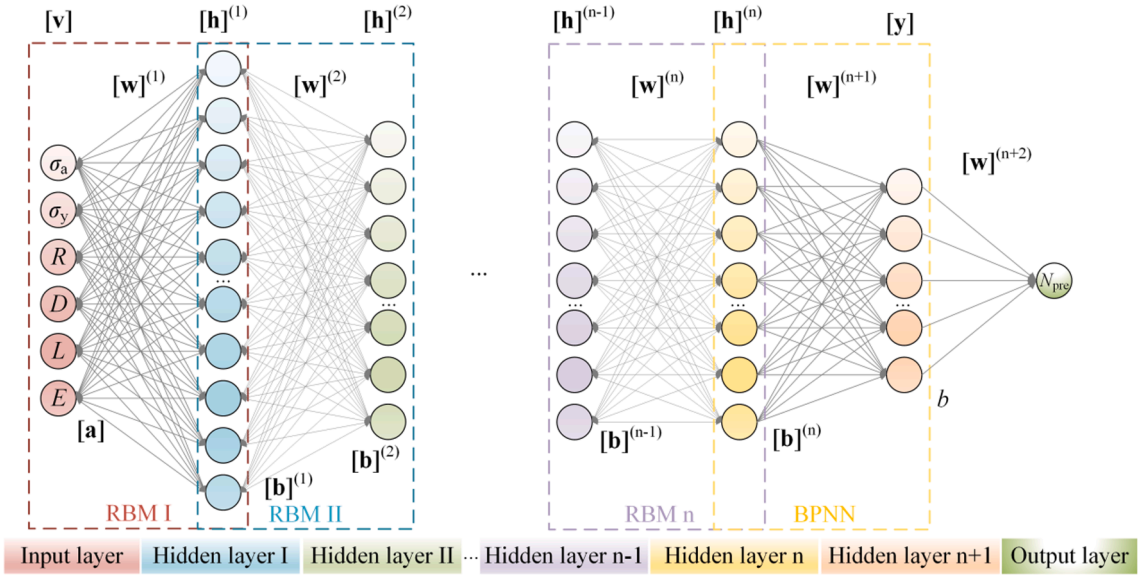

Fig. 5. The structure of a generic DBN-BP model.

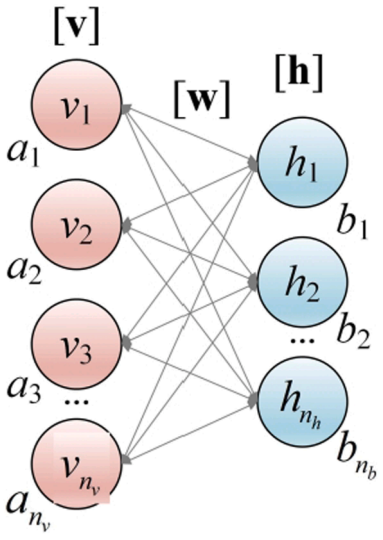

Fig. 6. The structure of a RBM.

minimized, the network reaches an ideal state. The network is trained to minimize this energy function of the network. Given a set of states (v, h), the energy function of RBM can be defined as [65]:

$$E(\mathbf{v},\mathbf{h}|\theta) = -\sum_{i=1}^{n_v} a_i v_i - \sum_{j=1}^{n_h} b_j h_j - \sum_{i=1}^{n_v}\sum_{j=1}^{n_h} h_j w_{ij} v_i \tag{8}$$

where $[\mathbf{v}] = [v_1, v_2, v_3, \ldots, v_{nv}]^{\mathrm{T}}$ is the input of the visible layer, $[\mathbf{h}] = [h_1, h_2, h_3, \ldots, h_{nh}]^{\mathrm{T}}$ is the output of the hidden layer, n_v and n_h are the number of neurons of the visible and hidden layers. $\theta = \{a_i, b_j, w_{ij}\}$ is the parameter of RBM, a_i and b_j are the biases of the visible and hidden layers, and w_{ij} is the weight between the two layers.

Then the joint probability distribution can be obtained and expressed as:

$$P(\mathbf{v},\mathbf{h}|\theta) = \frac{1}{Z(\theta)} e^{-E(\mathbf{v},\mathbf{h}|\theta)} \tag{9}$$

where, $Z(\theta) = \sum_{n_v,n_h} e^{-E(\mathbf{v},\mathbf{h}|\theta)}$ is the partition function.

The probabilities that neurons in the hidden and visible layers will be activated can be calculated and described as:

$$\begin{aligned} P(h_j = 1|\mathbf{v}) &= \frac{1}{1+\exp\left(-b_j - \sum_{i=1}^{n_v} v_i w_{ij}\right)} \\ P(v_i = 1|\mathbf{h}) &= \frac{1}{1+\exp\left(-a_i - \sum_{j=1}^{n_h} w_{ij} h_j\right)} \end{aligned} \tag{10}$$

RBMs are trained to maximize the likelihood function, i.e., the product of probabilities assigned to some training set V, denoted as $V = \{\mathbf{v}^1, \mathbf{v}^2, \ldots, \mathbf{v}^{ns}\}$ in which n_s represents the number of samples in the training set and the kth sample can be written as $\mathbf{v}^k = [v_1{}^k, v_2{}^k, \ldots, v_{nv}^k]^{\mathrm{T}}$. Thus, the likelihood function can be expressed as:

$$L(\theta) = \prod_{k=1}^{n_s} P(\mathbf{v}^k) \tag{11}$$

A maximum likelihood estimate was implemented to obtain the optimal values of the variable set $\theta = \{a_i, b_j, w_{ij}\}$ of RBM, by using the following equations:

$$\begin{aligned} \frac{\partial \log L(\theta)}{\partial w_{ij}} &= \sum_{k=1}^{n_s}[P(h_j = 1|\mathbf{v}^k)v_i^k - \sum_{k=1}^{n_s}[P(\mathbf{v}^k)P(h_j = 1|\mathbf{v}^k)v_i^k] \\ \frac{\partial \log L(\theta)}{\partial a_i} &= \sum_{k=1}^{n_s}[v_i^k - \sum_{v} P(\mathbf{v}^k)v_i^k] \\ \frac{\partial \log L(\theta)}{\partial b_j} &= \sum_{k=1}^{n_s}[P(h_j = 1|\mathbf{v}^k) - \sum_{k=1}^{n_s} P(\mathbf{v}^k)P(h_j = 1|\mathbf{v}^k)] \end{aligned} \tag{12}$$

Thereafter, a layered greedy algorithm is used to train every single layer, using the hidden layer of the current (ith) RBM as the visible layer of the next (($i+1$)th) RBM, such that the optimal values of variable set $\theta = \{a_i, b_j, w_{ij}\}$ can be obtained for every layer and the pre-training process is finished. Subsequently, based on local optimum results, the global optimization can be performed throughout the network to acquire the optimal values of variable set $\theta = \{a_i, b_j, w_{ij}\}$ for the entire network and the fine-tuning process is completed. With the integration of DBN and BPNN, the output of the DBN-BP model, i.e., the predicted fatigue life N_{pre}, can be well attained.

3.2.3. Optimization of hyperparameters

Hyperparameters are the parameters whose values are set manually in the deep learning model, rather than the model parameters obtained from the learning process, which mainly include number of hidden layers, number of nodes in hidden layers, batchsize, learning rate, epoch, etc. The number of hidden layers and hidden layer nodes determine the complexity of the neural network. An increase in these numbers can enhance the ability of the network to handle complex nonlinear problems but may result in a considerable elongation of time-consumption. The value of the batchsize should be in a reasonable range since a too small batchsize may lower the training speed and increase the difficulty of convergence, whereas a too large size may result in an inappropriate local minimum. The learning rate ought to be not too large to avoid the non-convergence of the prediction model and not too small to refrain a slow convergence rate and an excessive time-consumption. Epoch, similar to the iteration step, determines the fitting state of the model. The value of epoch should be increased to turn the prediction results from the initial underfitting state into the optimal fitting state, but may result in the overfitting state if the value of the epoch exceeds a threshold value. In brief, the training efficiency, prediction precision, generalization ability, and robustness of the network model are all closely related to the hyperparameters [66,67].

In order to obtain an excellent performance for the fatigue life prediction model, it is requisite to determine the appropriate values for these hyperparameters that are initialized before the training process. The initialization of the values of these hyperparameters usually are empirical and these values can be adjusted and optimized according to the comparison between the experimental results and the predicted results of the fatigue lives of LPBF-fabricated Ti-6Al-4V, so that the model has a superior prediction ability for any unseen data. Hyperparameters of BPNN and DBN-BP models were initialized and optimized and their values are listed in Tables 2 and 3, respectively.

3.3. Model evaluation

In order to comprehensively evaluate the fatigue life prediction models of LPBF-fabricated Ti-6Al-4V from various perspectives, three statistical measures, i.e., R^2 (coefficient of determination), RMSE (root mean square error) and MAE (mean absolute error), are employed to quantify the prediction precision of BPNN and DPN-BP models. The value of R^2 explicitly indicates how well the data fit the regression model in which the closer R^2 is to 1 means the model has a better prediction precision. RMSE clearly reflects the deviation between the predicted and experimental values in which a smaller value of RMSE represents a better prediction performance of the model. However, RMSE is quite sensitive to outliers because its calculation results are closely related to larger values. Thus, MAE is utilized to be the alternate of RMSE since it is not sensitive to the outliers. The smaller the value of MAE is, the higher the precision of the prediction model is. The expressions of R^2, RMSE and MAE are listed as follows.

$$R^2(y, y^{pre}) = 1 - \frac{\sum_{i=1}^{n}(y_i - y_i^{pre})^2}{\sum_{i=1}^{n}(y_i - y*)^2} \tag{13}$$

Table 2
Hyperparameter settings for the BPNN model.

Parameter	Value
Number of hidden layers	1
Number of nodes in hidden layer	10
Batchsize	32
Learning rate	0.01
Epoch	400

Table 3
Hyperparameter settings for the DBN-BP model.

Parameter	Value
Number of hidden layers	4
Number of nodes in Hidden layer I	10
Number of nodes in Hidden layer II	7
Number of nodes in Hidden layer III	7
Number of nodes in Hidden layer IV	5
Batchsize	32
Learning rate of pre-training	0.05
Epoch of pre-training	8
Learning rate of fine-tuning	0.05
Epoch of fine-training	2200

$$RMSE(y, y^{pre}) = \sqrt{\frac{1}{n}\sum_{i=1}^{n}(y_i - y_i^{pre})^2} \tag{14}$$

$$MAE(y, y^{pre}) = \frac{1}{n}\sum_{i=1}^{n}|y_i - y_i^{pre}| \tag{15}$$

where y_i denotes the ith experimental data, y_i^{pre} represents the ith predicted value, and y^* is the mean value of the experimental data.

4. Results and discussion

4.1. Fatigue life prediction results

For the purpose of comparison, both BPNN and DBN-BP models were employed to predict the fatigue life of LPBF-fabricated Ti-6Al-4V. The predicted values via the BPNN model were compared with the experimental values by using the data in the training, validation, and testing sets, which are shown in Figs. 7a, 7b and 7c, respectively. The comparisons of the predicted values via the DBN-BP model with the experimental values by using the data in the training, validation, and testing sets, are presented in Figs. 7d, 7e and 7f, respectively.

As seen in Fig. 7a, about 70% of prediction points are within the triple error band, whereas the remaining 30% of those points are outside the triple error band. Similarly, only 56% of prediction points are within the triple error band in Fig. 7b and 62% of the prediction values are within the triple error band in Fig. 7c. On the contrary, all the prediction points via the DBN-BP model are well within the triple error band and most of them fall on the isoline ($N_{pre} = N_f$), no matter of using the data in the training set, the validation set or the testing set (Figs. 7d-7f). It should also be noted that the majority of predicted fatigue lives of LPBF-fabricated Ti-6Al-4V by using the BPNN model are overvalued in HCF regime but undervalued in VHCF regime (shown in Figs. 7a-7c), whereas the prediction values via the DBN-BP model match the experimental values very well, in both HCF and VHCF regimes, by using the data in all three sets (illustrated in Figs. 7d-7f). The results in Fig. 7 clearly indicate that the DPN-BP model has a much better prediction precision than the BPNN model.

The above observations can be well explained by the characteristics of BPNN and DBN-BP models. When the BPNN model was utilized to predict the fatigue life of LPBF-fabricated Ti-6Al-4V, the input fatigue data were neither pre-processed nor further mined, which may cause the interaction between the data in HCF regime and the data in VHCF regime. When the fatigue lives in HCF regime were predicted, the prediction values were generally larger than the experimental values due to the effect of VHCF data. Similarly, when the fatigue lives in VHCF regime were predicted, the prediction values were usually smaller than the experimental values due to the effect of HCF data. On the other hand, the weights and biases obtained by the BPNN model make the prediction process tend to fall into the local optimum [18], causing the biased prediction results. As far as the DBN-BP model is concerned, it has the abilities of powerful reasoning and full description of relationships

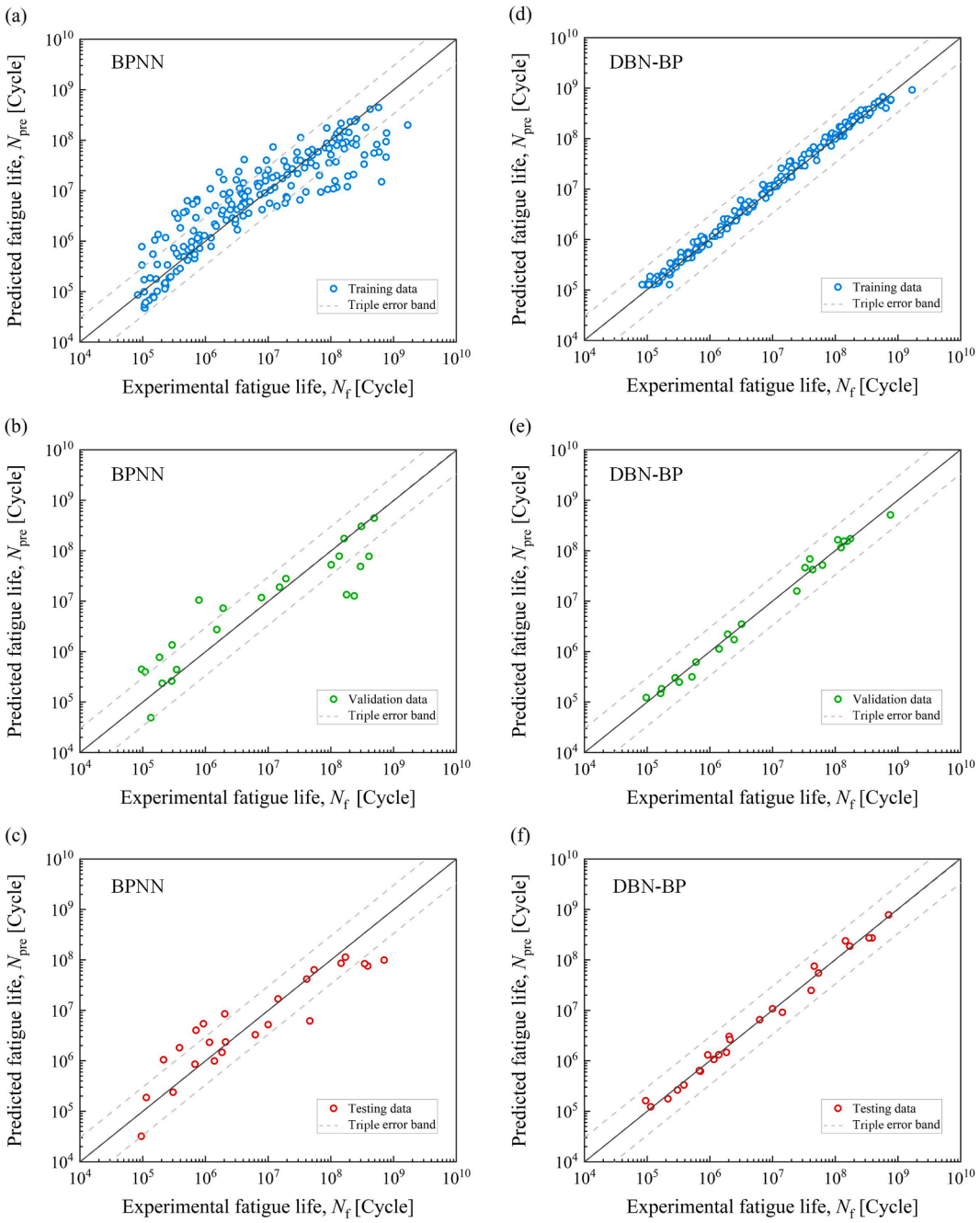

Fig. 7. Comparisons of experimental and predicted fatigue lives for (a) training set, (b) validation set and (c) testing set of the BPNN model; (d) training set, (e) validation set and (f) testing set of the DBN-BP model.

among input features [68], which can learn critical information from the input features of the dataset during the pre-training process [69], so as to avoid the influence of other irrelevant data on the prediction performance. With the combination of the pre-training and fine-tuning processes, the DBN-BP model is capable of obtaining better weights and biases than the BPNN model, making up for the shortcomings of the traditional BPNN model [70]. In brief, the DBN-BP model has exhibited the superior ability of predicting the fatigue life of LPBF-fabricated Ti-6Al-4V in both HCF and VHCF regimes.

4.2. Precision and stability of prediction models

In order to objectively and comprehensively evaluate the prediction performance of BPNN and DBN-BP models, the precision and stability of the prediction results obtained from both models were presented and compared. As stated in Section 3.3, three statistical measures, i.e., R^2, RMSE and MAE, were used to quantify the prediction precision of the BPNN and DPN-BP models. Figs. 8a and 8b present the values of R^2, RMSE and MAE via DBN-BP and BPNN models, by using the data of the training set, the validation set, and the testing set, respectively. It can be seen from Fig. 8 that the value of R^2 obtained from the DBN-BP model is consistently around 1, no matter of using the data of the training set, the validation set, or the testing set, which is much better than that from the BPNN model (about 0.8). Furthermore, the values of RMSE and MAE from the BPNN model are in the range of 0.4 ~ 0.5, which are far higher than those from the DBN-BP model (around 0.1). The comparisons of values of R^2, RMSE and MAE via DBN-BP and BPNN models clearly show that the DBN-BP model has a much better prediction performance than

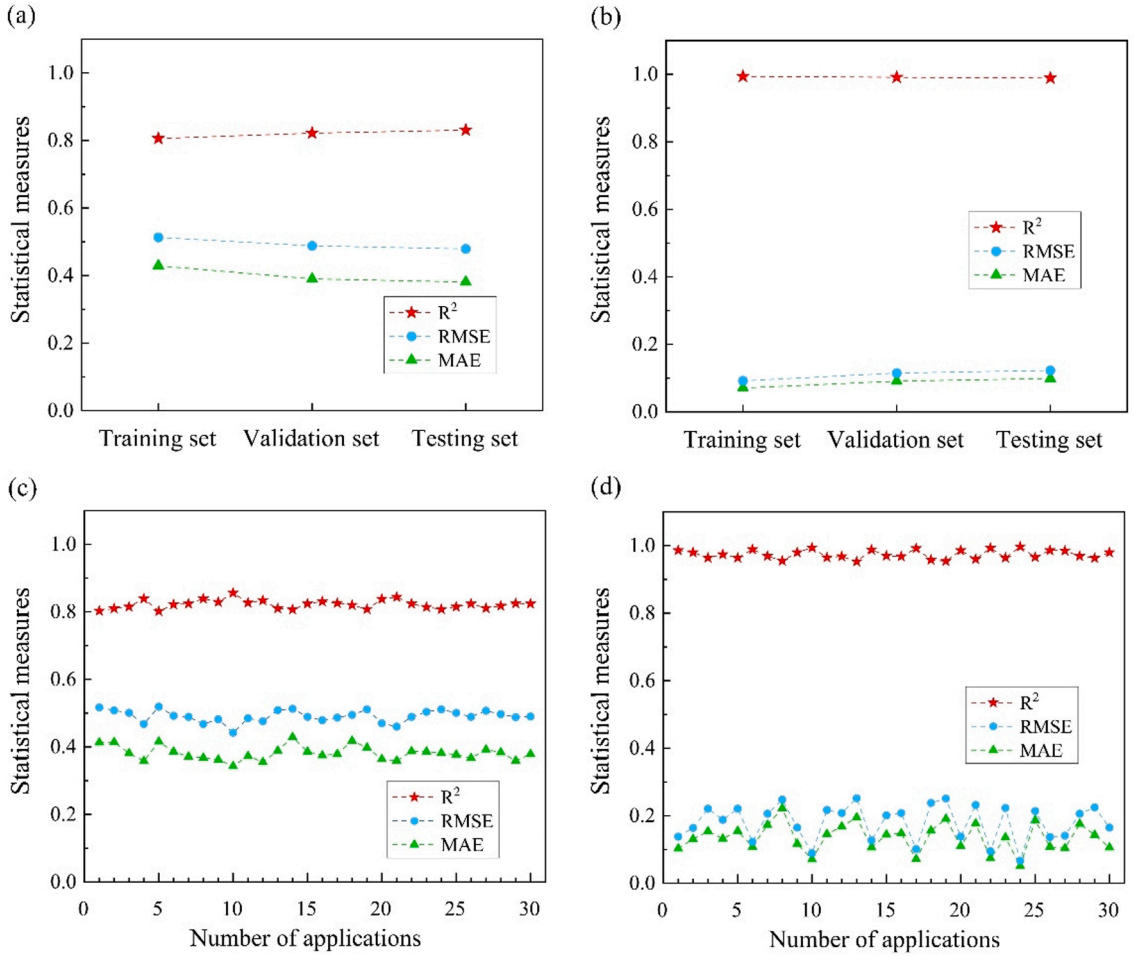

Fig. 8. Statistical measures of prediction precision for (a) BPNN and (b) DBN-BP models; Variation of statistical measures with repeated predictions from (c) BPNN and (d) DBN-BP models using the testing set.

the BPNN model. In addition, Figs. 8a and 8b illustrate that the values of R^2, MAE and RMSE for both DBN-BP and BPNN models vary in a relatively narrow range, regardless of using the data of the training set, the validation set, or the testing set, indicating that both models have not obvious overfitting and can be used to predict unseen data.

To be a superior prediction model, it is vital to have not only highly precise but strongly stable prediction performance. Therefore, the stability of these two prediction models was evaluated by repeated predictions using the prediction model under the same conditions. Figs. 8c and 8d show the variation of values of R^2, MAE and RMSE with 30 repeated predictions from BPNN and DBN-BP models by using the data in the testing set, respectively. It is seen that the values of R^2 have a small fluctuation (about 0.05) by using both BPNN and DBN-BP models. Nevertheless, the values of MAE and RMSE vary in a narrow range of 0.08 for the BPNN model but in a relatively wide range of 0.18 via the DBN-BP model which can be explained as follows. With the nearly-perfect fitting of the DBN-BP model, 30 times of repeated predictions may cause the amplification of the error/gap between the predicted value and the experimental value and consequently result in a relatively large fluctuation of the values of MAE and RMSE. Overall, both DBN-BP and BPNN models present excellent stability of predicting the fatigue life of LPBF-fabricated Ti-6Al-4V.

4.3. Analysis of hyperparameter sensitivity

Results in Sections 4.1 and 4.2 have clearly shown that both BPNN and DBN-BP models exhibited good fittings between the predicted and experimental values of the fatigue lives of LPBF-fabricated Ti-6Al-4V. In order to further optimize BPNN and DBN-BP models and verify the rationality of the hyperparameter settings in Tables 2 and 3, parametric studies were developed to analyze the sensitivity of hyperparameters. As the primary parameters directly affecting the prediction performance of neural network models [41,62], the number of hidden layers and number of nodes in each hidden layer were analyzed to optimize the predicted fatigue life of LPBF-fabricated Ti-6Al-4V in HCF and VHCF regimes by using BPNN and DBN-BP models.

First, the number of hidden layers were analyzed and optimized for both BPNN and DBN-BP models. Figs. 9a and 9b illustrate the variation of values of three statistical measures, i.e., R^2, RMSE and MAE, with the number of hidden layers (n_h) in the BPNN model and the DBN-BP model, respectively, by using the data of the testing set. In the BPNN model, the value of R^2 decreases slowly from 0.840 to 0.779 when n_h varies from 1 to 4, then drops steeply to 0 when n_h becomes 5. The value of RMSE increases slowly from 0.466 to 0.548 with n_h varying from 1 to 4, then rises rapidly to 1.168 when n_h reaches at 5. Similarly, the value of MAE grows slowly from 0.343 to 0.391 with n_h increasing from 1 to 4, then rises steeply to 1.031 when n_h becomes 5. In the DBN-BP model, the value of R^2 increases rapidly from 0.494 to 0.936 when n_h varies from 1 to 2, but increases slowly from 0.936 to 0.989 when n_h changes from 2 to 4, and keeps at 0.99 thereafter. The value of RMSE decreases steeply from 0.829 to 0.3 with n_h increasing from 1 to 2, then declines slowly to 0.123 with n_h varying from 2 to 4, and remains at around 0.1 afterwards. Similarly, the value of MAE drops quickly from 0.623 to 0.222 with n_h increasing from 1 to 2, then decreases slowly to 0.099 when n_h adds from

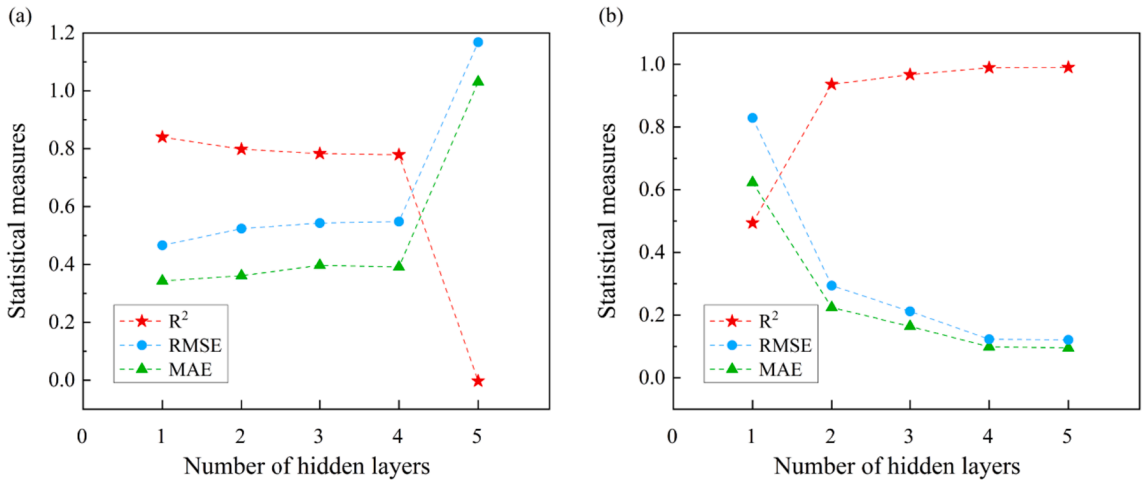

Fig. 9. Variation of statistical measures with the number of hidden layers in (a) the BPNN model and (b) the DPN-BP model by using the data in the testing set.

2 to 4, and stays at 0.08 afterwards.

The results in Fig. 9 evidently indicate that the number of hidden layers plays a significant role on the prediction precision of both BPNN and DBN-BP models. For the BPNN model, the prediction precision reaches the optimal value when the number of hidden layers is 1 and deteriorates steeply when the number of hidden layers becomes 5, inferring that the BPNN model is not suitable for deep learning. As far as the DBN-BP model is concerned, the prediction precision improves with the increase of the number of hidden layers and remain at the optimal value as long the number of hidden layers is no less than 4.

Second, the number of nodes in each hidden layer were analyzed and optimized for BPNN and DBN-BP models. According to the obtained optimization results, the number of hidden layers was chosen as 1 for the BPNN model and 4 for the DBN-BP model. The schemes of the parametric study of number of nodes in each hidden layer for BPNN and DBN-BP models are listed in Tables 4 and 5 respectively. Variations of the values of three statistical measures (R^2, RMSE and MAE) with the numbers of nodes in each hidden layer of BPNN and DBN-BP models are illustrated in Figs. 10 and 11, respectively.

As shown in Table 4, the BPNN model had only one hidden layer and the optimization begun with the number of nodes in the sole hidden layer varying from 5 to 25 with an increment of 5. Fig. 10 indicates that the values of all three statistical measures (R^2, RMSE and MAE) converge quickly when the number of nodes reaches to 10 and fluctuates in a very narrow range afterwards, inferring the optimal value of the number of nodes being 10 for the BPNN model with a single hidden layer.

For the DBN-BP model, as shown in Table 5, the optimization begun with the number of nodes in the first hidden layer while keeping the nodes of other hidden layers unchanged. Once the number of nodes in hidden layer I was optimized, then the number of nodes in hidden layer II would be optimized while keeping the nodes of other hidden layers constant. Similarly, the numbers of nodes in hidden layers III and IV could be optimized. Figs. 11a-d show the variations of the values of three statistical measures (R^2, RMSE and MAE) with the numbers of nodes in hidden layers I ~ IV by using the data in the testing set, respectively. It can be seen in Table 5 that the optimization begun with the number of nodes in the first hidden layer varying from 5 to 25 with an increment of 5, while keeping the nodes of other hidden layers unchanged. Results in Fig. 11a show that the values of all three statistical measures (R^2, RMSE and MAE) fluctuate in a very narrow range after the number of nodes in hidden layer I reaches at 10, inferring the optimal value of the number of nodes in the first hidden layer being 10. Then the number of nodes in the hidden layer II varied from 2 to 22 with an increment of 5 while keeping the number of nodes in other hidden layers constant. Fig. 11b indicates that the optimal value of the number of nodes in hidden layer II is 10 since the values of R^2, RMSE and MAE vary very little after the number of nodes in hidden layer II becomes 7. Nevertheless, Figs. 11c and 11d reveal that the variations of the number of nodes in hidden layers III and IV have little effect on the prediction precision of the DBN-BP model.

Table 4
Scheme of parametric study for number of nodes in the BPNN model.

Number of hidden layers	1	1	1	1	1
Number of nodes	5	10	15	20	25

Table 5
Scheme of parametric study for number of nodes in the DBN-BP model.

Hidden layer	I	II	III	IV
Number of nodes	5, 10, 15, 20, 25	7	7	5
	10	2, 7, 12, 17, 22	7	5
	10	7	2, 7, 12, 17, 22	5
	10	7	7	5, 10, 15, 20, 25

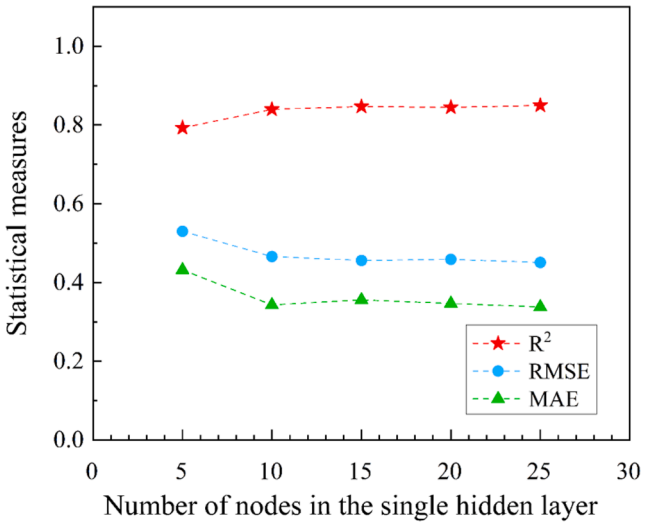

Fig. 10. Values of statistical measures versus the number of nodes in the BPNN model with a single hidden layer, by using data in the testing set.

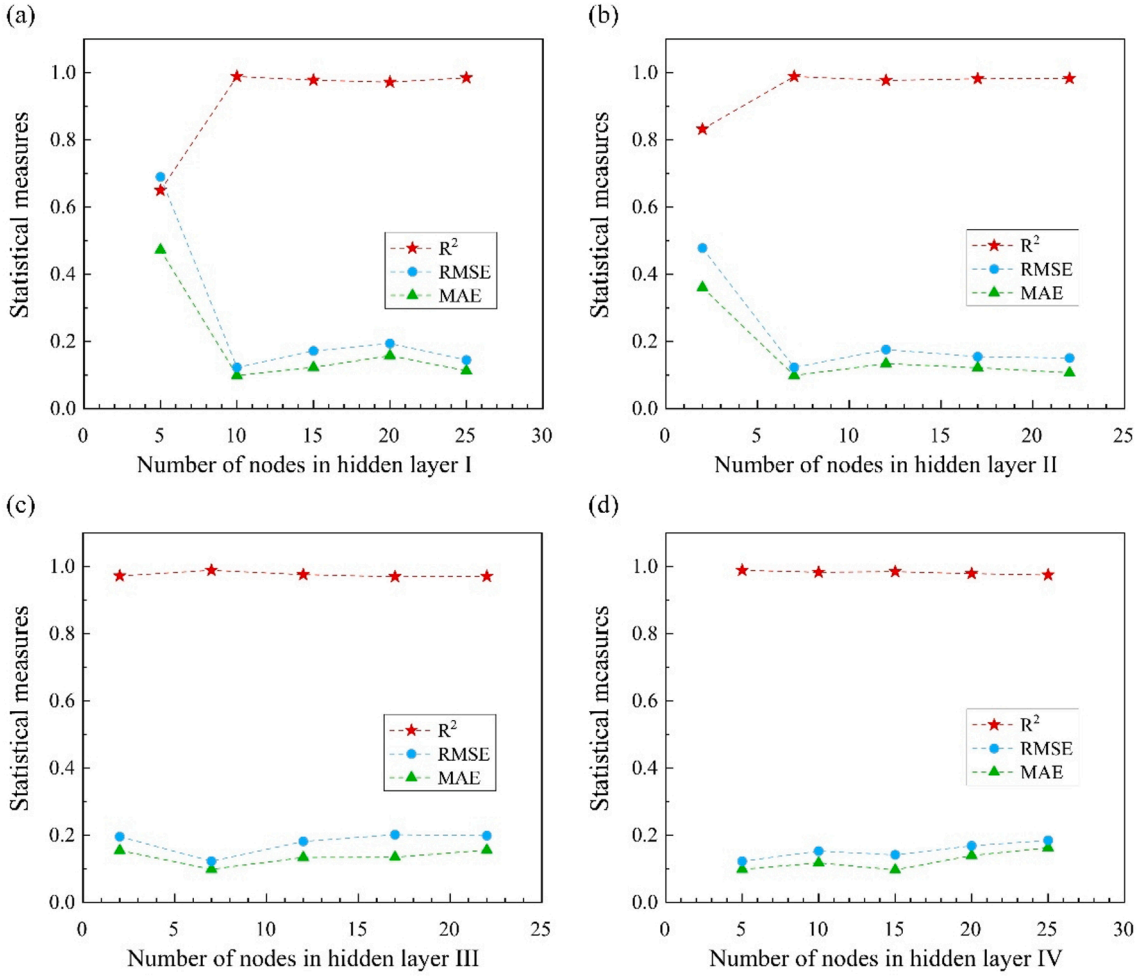

Fig. 11. Values of statistical measures versus the number of nodes in (a) hidden layer I, (b) hidden layer II, (c) hidden layer III, and (d) hidden layer IV in the DBN-BP model, via the use of the data in the testing set.

The numbers of nodes in hidden layers III and IV should be chosen as 7 and 5, respectively, to have the largest R^2 and smallest RMSE and MAE. Based on the above discussion, it is evident that the prediction precision mainly depends on the number of hidden layers and the number of nodes on the first two hidden layers of the DBN-BP model. The rationality of the hyperparameter settings in Tables 2 and 3 was also verified by the optimization results.

4.4. Applications of the DBN-BP model

As shown in Sections 4.1–4.3, the DBN-BP model has high precision and strong stability in fatigue life prediction of LPBF-fabricated Ti-6Al-4V. In this section, it is applied to predict several aspects of the fatigue behavior of LPBF-fabricated Ti-6Al-4V.

First, the DBN-BP model is applied to predict the relation between the stress amplitude and the mean stress of LPBF-fabricated Ti-6Al-4V in both HCF and VHCF regimes. As stated in Ref. [53], the relation between stress amplitude and mean stress of LPBF-fabricated Ti-6Al-4V was correlated by the models of Gerber [71], Goodman [72] and Pan et al. [73] as expressed in Eqs. (16)–(18), respectively, in which σ_a is the applied stress amplitude, σ_{-1} is the fatigue strength at $R = -1$, σ_m is the mean stress and σ_u is the tensile strength of tested material.

Gerber formula:

$$\sigma_a = \sigma_{-1}\left[1 - \left(\frac{\sigma_m}{\sigma_u}\right)^2\right] \tag{16}$$

Goodman formula:

$$\sigma_a = \sigma_{-1}\left(1 - \frac{\sigma_m}{\sigma_u}\right) \tag{17}$$

Pan et al. formula:

$$\sigma_a = \sigma_{-1}\left(1 - \frac{\sigma_m}{\sigma_u}\right)^2 \tag{18}$$

By using Eqs. (16)–(18), Haigh diagrams were obtained and illustrated in Fig. 12 to show the relation between σ_m and σ_a for HCF ($N_f = 10^6$) and VHCF ($N_f = 10^8$) of the tested LPBF-fabricated Ti-6Al-4V specimens, in which $\sigma_b = 1246$ MPa, $\sigma_{-1} = 220$ MPa for HCF regime and $\sigma_{-1} = 150$ MPa for VHCF regime [53]. However, it is seen that none of the curves generated by these three models are close to experimental data under any stress ratio, indicating they cannot be used to estimate the relation between stress amplitude and mean stress of LPBF-fabricated Ti-6Al-4V in both HCF and VHCF regimes.

Then the DBN-BP model was utilized to predict the relation between stress amplitude and mean stress of LPBF-fabricated Ti-6Al-4V under various stress ratios. For the purpose of comparison, the values of input features σ_y, D, L and E were set as the same values in Ref [53], i.e., 1191 MPa, 3.5 mm, 45 μm, and 69 J/mm^3, respectively. By varying the values of input values σ_a and R, various fatigue lives of LPBF-fabricated Ti-6Al-4V were predicted and the relations between σ_m and σ_a for HCF ($N_f = 10^6$) and VHCF ($N_f = 10^8$) are illustrated in Figs. 12a and 12b, respectively. It is seen that the prediction curve generated by the DBN-BP

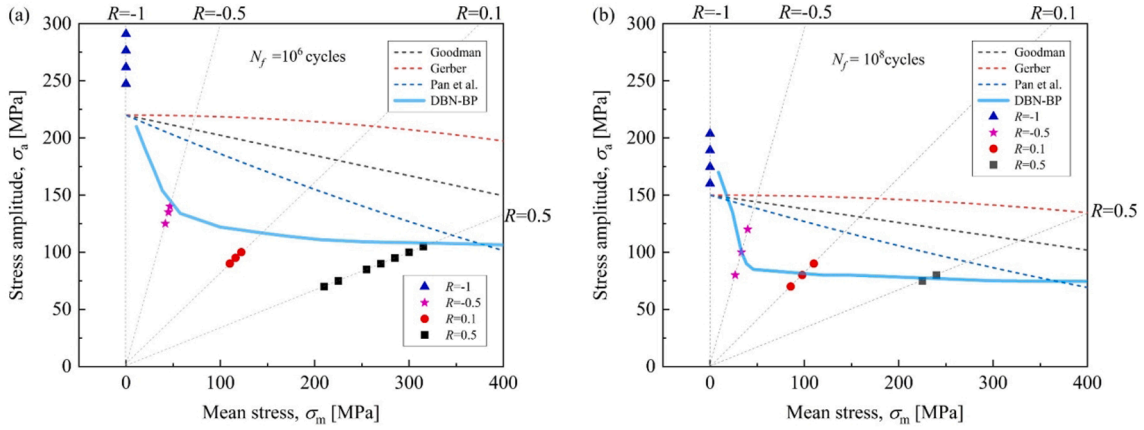

Fig. 12. Haigh diagrams of LPBF-fabricated Ti6Al-4V showing the relation of mean stress and stress amplitude at (a) $N_f = 10^6$ cycles and (b) $N_f = 10^8$ cycles.

model matches well with the experimental data in both HCF and VHCF regimes. As stated in previous sections, with the combination of pre-training and fine-tuning processes, the DBN-BP model is able to extract and transform fatigue-relevant input features into the model such that the weights and biases of the model are optimized and consequently the prediction performance is considerably enhanced.

Second, the DBN-BP model was employed to predict the effect of the input feature E on the fatigue performance of LPBF-fabricated Ti-6Al-4V in HCF and VHCF regimes. The effects of processing parameters on the fatigue behavior of LPBF-fabricated Ti-6Al-4V had been experimentally investigated by our group and published in Ref. [58]. In order to compare with the experimental results in Ref. [58], the values of input features D, L and R of the DBN-BP model were set as the same values in Ref [58], i.e., D = 3.5 mm, L = 34 μm and R = − 1. In order to distinguish the effect of E on the fatigue performance of LPBF-fabricated Ti-6Al-4V from the effect of σ_y, the value of σ_y was constrained in a narrow range of 1100 ~ 1200 MPa. Thus, only the input data of groups 1, 2, 4, and 5 in Table 1 were adopted, with the values of σ_y are 1176, 1117, 1135, and 1189 MPa, and the values of E are 47.6, 26.7, 41.0, and 63.5 J/mm^3, respectively. For the purpose of comparison, the BPNN model was also utilized to obtain the prediction results with same input data. Fig. 13 shows the comparison of predicted values by DBN-BP and BPNN models and experimental data of fatigue lives of LPBF-fabricated Ti-6Al-4V for each group. In order to distinguish the "unseen/blinded" data in the testing set and the "used" data in training and validation sets, hollow spots were utilized to represent the "unseen/blinded" testing data and solid spots were employed to denote the "used" training and validation data. Comparison indicates that the DBN-BP model exhibits a better prediction performance than the BPNN model, no matter using the "used" data in training and validation sets, or the "unseen/blinded" data in the testing set. It is seen that the overall fatigue strength in HCF and VHCF regimes gets larger with the increase of energy density E and reaches the largest value at E = 47.6 J/mm^3 (group 1), then decreases rapidly when E = 63.5 J/mm^3 (group 5), implying that the fatigue strength of LPBF-fabricated Ti-6Al-4V is not linearly related with the magnitude of energy density E.

Third, it is interesting to note that groups 1 and 9 have the same value of E (47.6 J/mm^3) but different values of σ_y (1176 and 1089 MPa). Hence, the S-N curve was predicted by DBN-BP and BPNN models using the input data of group 9 in Table 1, and the comparison of predicted values by DBN-BP and BPNN models and experimental values of the fatigue lives of LPBF-fabricated Ti-6Al-4V for groups 1 and 9 is presented in Fig. 14 in which solid spots represent the "used" data in training and validation sets and hollow spots denote the "unseen/blinded" data in the testing set. It can be seen again that the prediction performance of the DBN-BP model is better than that of the BPNN model, no matter comparing with the "used" data in training and validation sets or the "unseen/blinded" data in the testing set. Furthermore, it is seen that

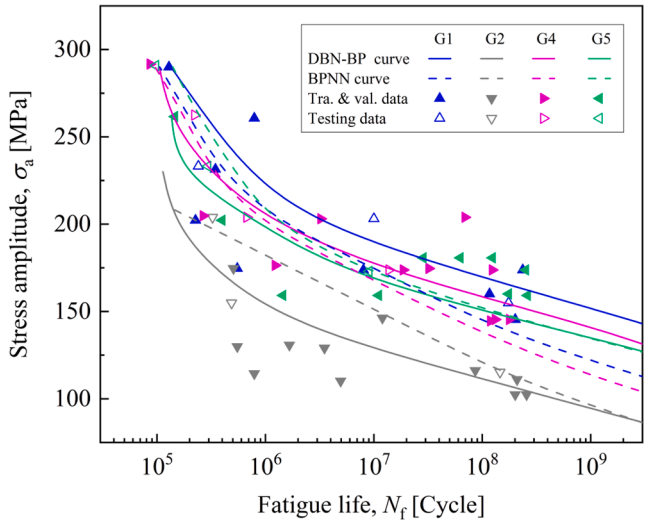

Fig. 13. Comparison of experimental data and prediction results by DBN-BP and BPNN models of LPBF-fabricated Ti-6Al-4V, using input data of groups 1, 2, 4, 5.

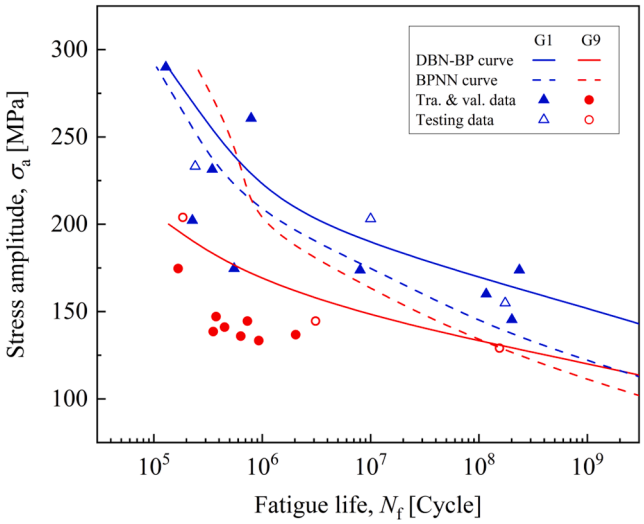

Fig. 14. Comparisons of experimental data and prediction results by DBN-BP and BPNN models of LPBF-fabricated Ti-6Al-4V, using input data of groups 1 and 9.

fatigue strength of group 1 ($\sigma_y = 1176$ MPa) is higher than that of group 9 ($\sigma_y = 1089$ MPa), inferring that the fatigue strength gets larger with the increase of the yield strength under the same value of the energy density.

5. Conclusions

In this paper, a deep learning model, named the DBN-BP model, was proposed to predict the fatigue life of LPBF-fabricated Ti-6Al-4V up to VHCF regime by integrating DBN as the pre-training process and BPNN as the fine-tuning process. The main conclusions of this paper are listed as follows.

(1) Comparison with the experimental data clearly indicates that the DBN-BP model presents a much better performance ($R^2 \cong 0.99$, RSME and MAE $\cong$ 0.1) than the BPNN model ($R^2 \cong 0.8$, RSME $\cong$ 0.5, and MAE $\cong$ 0.4) in fatigue life prediction of LPBF-fabricated Ti-6Al-4V, which evidently validates the correctness and precision of the DBN-BP model. The stability of the DBN-BP model is also verified since values of R^2 fluctuate in a very narrow range between 0.9 and 1 after 30 times of repeated predictions from the DBN-BP model under the same conditions.

(2) The BPNN model with a single hidden layer has the optimal prediction precision and the optimal number of hidden layers in the DBN-BP model is 4. The optimal number of nodes in the first and second hidden layer should be 10 and 7, respectively, to reach the optimum and stable values for the three statistical measures of the DBN-BP model. Nevertheless, variations of the number of nodes in the hidden layers III and IV have little effect on the prediction precision of the DBN-BP model.

(3) The DBN-BP model exhibits a significantly better performance in predicting the relation between mean stress and stress amplitude than other proposed empirical models. The prediction curve agrees very well with the experimental data in both HCF and VHCF regimes of LPBF-fabricated Ti-6Al-4V. Prediction results by using the DBN-BP model revealed that energy density E has a direct impact on the fatigue strength of LPBF-fabricated Ti-6Al-4V, but not in a linear relationship.

The above findings provide a comprehensive insight into the deep learning-based fatigue life prediction model of LPBF-fabricated Ti-6Al-4V up to VHCF regime. The prediction performance of the DBN-BP model could be further enhanced if more fatigue-relevant input features were considered, such as the variable amplitude fatigue test, the location, size and distribution of defects. In addition, this DBN-BP model could be employed to future prediction on the fatigue lives of other commonly-used additive manufactured alloys such as SS 316L and AlSi10Mg.

Declaration of competing interest

The authors declare that they have no known competing financial interests or personal relationships that could have appeared to influence the work reported in this paper.

Data availability

The data that support the findings of this study are available from the authors upon reasonable request.

Acknowledgments

This work was supported by Guangdong basic and applied basic research foundation (Grant No. 2019A1515110758), Shenzhen municipal science and technology innovation council (Grant No. ZDSYS20210616110000001), Hunan provincial leading talents program in science and technology innovations (2021RC4051), and the National Natural Science Foundation of China (No. 11932020).

References

[1] Bao H, Wu S, Wu Z, Kang G, Peng X, Withers P. A machine-learning fatigue life prediction approach of additively manufactured metals. Eng Fract Mech 2021;242:107508.
[2] Hor as J, B hal J, Homola P, Senck S, Holzleitner M, Godja N, Pásztor Z, Hegedüs B, Doubrava R, Rů ek R, Petrusová L. Modelling fatigue life prediction of additively manufactured Ti-6Al-4V samples using machine learning approach. Int J Fatigue 2023; 169: 107483.
[3] Konda N, Verma R, Jayaganthan R. Machine learning based predictions of fatigue crack growth rate of additively manufactured Ti6Al4V. Metals 2022;12:50.
[4] Zhan Z, Li H. Machine learning based fatigue life prediction with effects of additive manufacturing process parameters for printed SS 316L. Int J Fatigue 2021;142:105941.
[5] Pandey V, Singh I, Mishra B, Ahmad S, Rao A, Kumar V. A new framework based on continuum damage mechanics and XFEM for high cycle fatigue crack growth simulations. Eng Fract Mech 2019;206:172–200.
[6] Sandoval C, Malcher L, Canut F, Araújo L, Doca T, Araújo J. Micromechanical Gurson-based continuum damage under the context of fretting fatigue: Influence of the plastic strain field. Int J Plasticity 2020;125:235–64.
[7] Tridello A, Niutta C, Berto F, Qian G, Paolino D. Fatigue failures from defects in additive manufactured components: A statistical methodology for the analysis of the experimental results. Fatigue Fract Eng Mater Struct 2021;44:1944–60.
[8] Burr A, Persenot T, Doutr P, Buffiere J, Lhuissier P, Martin G, et al. A numerical framework to predict the fatigue life of lattice structures built by additive manufacturing. Int J Fatigue 2020;139:105769.
[9] Haridas R, Thapliyal S, Agrawal P, Mishra R. Defect-based probabilistic fatigue life estimation model for an additively manufactured aluminum alloy. Mat Sci Eng A-Struct 2020;798:140082.
[10] Gan L, Wu H, Zhong Z. On the use of data-driven machine learning for remaining life estimation of metallic materials based on Ye-Wang damage theory. Int J Fatigue 2022;156:106666.
[11] Liu Y, Wu J, Wang Z, Lu X-G, Avdeev M, Shi S, et al. Predicting creep rupture life of Ni-based single crystal superalloys using divide-and-conquer approach based machine learning. Acta Mater 2020;195:454–67.
[12] Zhang X, Gong J, Xuan F. A physics-informed neural network for creep-fatigue life prediction of components at elevated temperatures. Eng Fract Mech 2021;258:108130.
[13] Vassilopoulos AP, Georgopoulos EF, Dionysopoulos V. Artificial neural networks in spectrum fatigue life prediction of composite materials. Int J Fatigue 2007;29(1):20–9.
[14] Dang L, He X, Tang D, Li Y, Wang T. A fatigue life prediction approach for laser-directed energy deposition titanium alloys by using support vector regression based on pore-induced failures. Int J Fatigue 2022;159:106748.
[15] Liu Q, Shi W, Chen Z. Rubber fatigue life prediction using a random forest method and nonlinear cumulative fatigue damage model. J Appl Polym Sci 2020;137:48519.
[16] Gan L, Wu H, Zhong Z. Fatigue life prediction considering mean stress effect based on random forests and kernel extreme learning machine. Int J Fatigue 2022;158:106761.
[17] Dedeakayogulları H, Kaçal A, Keser K. Modeling and prediction of surface roughness at the drilling of SLM-Ti6Al4V parts manufactured with pre-hole with optimized ANN and ANFIS. Measurement 2022;203:112029.
[18] Niu G, Yi X, Chen C, Li X, Han D, Yan B, et al. A novel effluent quality predicting model based on genetic-deep belief network algorithm for cleaner production in a full-scale paper-making wastewater treatment. J Clean Prod 2020;265:121787.
[19] Chu J, Liu X, Zhang Z, Zhang Y, He M. A novel method overcoming overfitting of artificial neural network for accurate prediction: Application on thermophysical property of natural gas. Case Stu Therm Eng 2021;28:101406.
[20] Liang R, Yu R, Zhang Y. Machine learning of weld joint penetration from weld pool surface using support vector regression. J Manuf Process 2019;41:23–8.
[21] Li J, Zhu D, Li C. Comparative analysis of BPNN, SVR, LSTM, Random Forest, and LSTM-SVR for conditional simulation of non-Gaussian measured fluctuating wind pressures. Mech Syst Signal Pr 2022;178:109285.
[22] Xu H, Wang R, Wang K. A new SVR incremental algorithm based on boundary vector. CiSE Wuhan, China 2010: 11706831.
[23] Lu S, Chen Y, Zhu X, Wang Z, Ou Y, Xie Y. Exploring support vector machines for big data analyses. CSSE 2021:31–7.
[24] Shi Y, Wang S, Jiang Y, Liu P. Transfer learning support vector regression. J Comp Appl 2013;33:3084–9.
[25] Zhang S, Zhou Y, Yan J, Bu F. Missing data completion method based on KNN and Random Forest. 2nd IYSF Academic Symposium on Artificial Intelligence and Computer Engineering, 2021: 12079.
[26] Yu Z, Zhang C, Xiong N, Chen F. A new random forest applied to heavy metal risk assessment. CSSE 2022;40:207–21.
[27] Sun Z, Sun H, Zhang J. Multistep wind speed and wind power prediction based on a predictive deep belief network and an optimized random forest. Math Probl Eng 2018;2018:1–16.
[28] Li G, Chandra S, Rashid R, Palanisamy S, Ding S. Machinability of additively manufactured titanium alloys: A comprehensive review. J Manuf Process 2022;75:72–99.
[29] Zhang J, Liu Y, Sha G, et al. Designing against phase and property heterogeneities in additively manufactured titanium alloys. Nat commun 2022;13:4660.
[30] Ladani L, Sadeghilaridjani M. Review of powder bed fusion additive manufacturing for metals. Metals 2021;11:1391.

[31] Lewandowski JJ, Seifi M. Metal additive manufacturing: A review of mechanical properties. Annu Rev Mater Res 2016;46:151–86.
[32] Shipley H, McDonnell D, Coull R, Lupoi R, O'Donnell G, Trimble D. Optimisation of process parameters to address fundamental challenges during selective laser melting of Ti-6Al-4V: A review. Int J Mach Tools Manuf 2018;128:1–20.
[33] Nguyen DS, Park HS, Lee CM. Optimization of selective laser melting process parameters for Ti-6Al-4V alloy manufacturing using deep learning. J Manuf Process 2020;55:230–5.
[34] Sanaei N, Fatemi A. Analysis of the effect of surface roughness on fatigue performance of powder bed fusion additive manufactured metals. Theor Appl Fract Mech 2020;108:102638.
[35] Gong H, Rafi K, Gu H, Janaki Ram GD, Starr T, Stucker B. Influence of defects on mechanical properties of Ti-6Al-4V components produced by selective laser melting and electron beam melting. Mater Des 2015;86:545–54.
[36] Li P, Warner DH, Fatemi A, Phan N. Critical assessment of the fatigue performance of additively manufactured Ti-6Al-4V and perspective for future research. Int J Fatigue 2016;85:130–43.
[37] Masuo H, Tanaka Y, Morokoshi S, Yagura H, Uchida T, Yamamoto Y, et al. Influence of defects, surface roughness and HIP on the fatigue strength of Ti-6Al-4V manufactured by additive manufacturing. Int J Fatigue 2018;117:163–79.
[38] Borrego LP, Jesus J, Ferreira JAM, Costa JDM, Capela C. Assessment of the fatigue performance of heat-treated addictive manufactured Ti-6Al-4V specimens. Procedia Struct Integr 2019;18:651–6.
[39] Yu H, Li F, Wang Z, Zeng X. Fatigue performances of selective laser melted Ti-6Al-4V alloy: Influence of surface finishing, hot isostatic pressing and heat treatments. Int J Fatigue 2019;120:175–83.
[40] Zhan Z, Hu W, Meng Q. Data-driven fatigue life prediction in additive manufactured titanium alloy: A damage mechanics based machine learning framework. Eng Fract Mech 2021;252:107850.
[41] Li J, Yang Z, Qian G, Berto F. Machine learning based very-high-cycle fatigue life prediction of Ti-6Al-4V alloy fabricated by selective laser melting. Int J Fatigue 2022;158:106764.
[42] Hong Y, Sun C. The nature and the mechanism of crack initiation and early growth for very-high-cycle fatigue of metallic materials - An overview. Theor Appl Fract Mec 2017;92:331–50.
[43] Sakai T, Oguma N, Morikawa A. Microscopic and nanoscopic observations of metallurgical structures around inclusions at interior crack initiation site for a bearing steel in very high-cycle fatigue. Fatigue Fract Eng Mater Struct 2015;38:1305–14.
[44] Heinz S, Eifler D. Crack initiation mechanisms of Ti-6Al-4V in the very high cycle fatigue regime. Int J Fatigue 2016;93:301–8.
[45] Ma H, Cheng X. A method for unbalanced big data classification based on optimization random forest. Microelectronics Computer 2018;35:28–32.
[46] Banki M, Shirazi A. Using wavelet support vector machine for classification of hyperspectral images. 2009 Second International Conference on Machine Vision: 154–157.
[47] Yang J, Kang G, Liu Y, Kan Q. A novel method of multiaxial fatigue life prediction based on deep learning. Int J Fatigue 2021;151:106356.
[48] Maleki E, Unal O, Sahebari S, Kashyzadeh K, Danilov I. Application of deep neural network to predict the high-cycle fatigue life of AISI 1045 steel coated by industrial coatings. J Mar Sci Eng 2022;10:128.
[49] Hinton G, Osindero S, Teh Y. A fast learning algorithm for deep belief nets. Neural Comput 2006;18(7):1527–54.
[50] Hinton G. Deep belief networks Scholarpedia 2009;4(6):5947.
[51] Liu SY, Shin YC. Additive manufacturing of Ti-6Al-4V alloy: A review. Mater Des 2019;164:107552.
[52] Gong H, Rafi K, Gu H, Starr T, Stucker B. Analysis of defect generation in Ti-6Al-4V parts made using powder bed fusion additive manufacturing processes. Addit Manuf 2014;1:87–98.
[53] Fu R, Zheng L, Ling C, Zhong Z, Hong Y. An experimental investigation of fatigue performance and crack initiation characteristics for an SLMed Ti-6Al-4V under different stress ratios up to very-high-cycle regime. Int J Fatigue 2022;164:107119.
[54] Fu R, Zheng L, Zhong Z, Hong Y. High-cycle and very-high-cycle fatigue behavior at two stress ratios of Ti-6Al-4V manufactured via laser powder bed fusion with different surface states. Fatigue Fract Eng Mater Struct 2023:1–16. https://doi.org/10.1111/ffe.13985.
[55] Fotovvati B, Namdari N, Dehghanghadikolaei A. Fatigue performance of selective laser melted Ti-6Al-4V components: State of the art. Mater Res Express 2019;6:012002.
[56] Günther J, Krewerth D, Lippmann T, Leuders S, Tröster T, Weidner A, et al. Fatigue life of additively manufactured Ti-6Al-4V in the very high cycle fatigue regime. Int J Fatigue 2017;94:236–45.
[57] Qian G, Li Y, Paolino DS, Tridello A, Berto F, Hong Y. Very-high-cycle fatigue behavior of Ti-6Al-4V manufactured by selective laser melting: Effect of build orientation. Int J Fatigue 2020;136:105628.
[58] Du L, Qian G, Zheng L, Hong Y. Influence of processing parameters of selective laser melting on high-cycle and very-high-cycle fatigue behaviour of Ti-6Al-4V. Fatigue Fract Eng Mater Struct 2021;44:240–56.
[59] Du L, Pan X, Qian G, Zheng L, Hong Y. Crack initiation mechanisms under two stress ratios up to very-high-cycle fatigue regime for a selective laser melted Ti-6Al-4V. Int J Fatigue 2021;149:106294.
[60] Thijs L, Verhaeghe F, Craeghs T, Van Humbeeck J, Kruth J. A study of the microstructural evolution during selective laser melting of Ti–6Al–4V. Acta Mater 2010;58:3303–12.
[61] Github: https://github.com/Jxinyee/dbn_pytorch.
[62] Park JM, Kang HT. Prediction of fatigue life for spot welds using back-propagation neural networks. Mater Des 2007;28(10):2577–84.
[63] Oostwal E, Straat M, Biehl M. Hidden unit specialization in layered neural networks: ReLU vs. sigmoidal activation. Cornell University Press, 2021.
[64] He J, Li L, Xu J. ReLU deep neural networks from the hierarchical basis perspective. Comput Math Appl 2022;120:105–14.
[65] Fischer A, Igel C. An introduction to restricted boltzmann machines. Lecture Notes in Computer Science, vol 7441. Springer, Berlin, Heidelberg; 2012.
[66] Schilling N, Wistuba M, Drumond L, Schmidt-Thieme L. Joint model choice and hyperparameter optimization with factorized multilayer perceptrons. 27th IEEE International Conference on Tools with Artificial Intelligence, 2015: 72–79.
[67] Chatzimparmpas A, Martins RM, Kucher K, Kerren A. Visual analytics to support hyperparameter search through evolutionary optimization. Comput Graph Forum 2021;40:201–14.
[68] Su X, Cao C, Zeng X, Feng Z, Shen J, Yan X, et al. Application of DBN in analog circuit fault diagnosis. Sci Rep-UK 2021;11:7969.
[69] Zhang K, Shi S, Liu S,Wan J, Ren L. Research on DBN-based evaluation of distribution network reliability. 7th International Conference on Renewable Energy Technologies 2021; 242: 03004.
[70] Xue H, Yang J, Tan K. Application of an improved BP neural network in handwriting recognition. Elec Sci Tech 2015;28:20–3.
[71] Gerber H. Bestimmung der zulässigen Spannungen in Eisenkonstructionen. Zeitschrift des Bayerischen Architeckten and Ingenieur-Vereins 1874;6:101–10.
[72] Goodman J. Mechanics Applied to Engineering. London: Longmans Green, 1899.
[73] Pan X, Su H, Sun C, Hong Y. The behavior of crack initiation and early growth in high-cycle and very-high-cycle fatigue regimes for a titanium alloy. Int J Fatigue 2018;115:67–78.